USING MAGNETIC RESONANCE IMAGING TO TRACK INFLAMMATORY CELLS IN A MURINE MYOCARDIAL INFARCTION MODEL

A Thesis
Presented to
The Academic Faculty

By

Yidong Yang

In Partial Fulfillment
Of the Requirement for the Degree
Master of Science in Medical Physics

Georgia Institute of Technology

May 2009

USING MAGNETIC RESONANCE IMAGING TO TRACK INFLAMMATORY CELLS IN A MURINE MYOCARDIAL INFARCTION MODEL

Approved by:

Dr. Tom C.-C. Hu, Advisor
Department of Radiology
Medical College of Georgia

Dr. Sang H. Cho, Coadvisor
School of Mechanical Engineering
Georgia Institute of Technology

Dr. Chris C.-K. Wang
School of Mechanical Engineering
Georgia Institute of Technology

Dr. Nathan E. Yanasak
Department of Radiology
Medical College of Georgia

Date Approved: 11/24/2008

ACKNOWLEDGEMENTS

I wish to thank Dr. Tom C.-C. Hu for his instruction and advice in the research and his careful reviewing and revising in forming this thesis. I would also like to thank the MCG Small Animal Imaging group. Dr. Nathan Yanasak, Benjamin Waghorn, Stephanie Jacob, Jimei Liu and Chris Middletown provided many helpful suggestions. I also got a lot of help from the MCG cancer research center. Dr. Nahid Mivechi and Caixia Xi helped a lot in processing the animal samples for histology. Last but not least, I would like to give my special thanks to Yuhui Yang for her hard work with the animal surgery. Without the help from all these nice people, this thesis can not be done.

TABLE OF CONTENTS

LIST OF TABLES

LIST OF FIGURES

LIST OF ABBREVIATIONS

CNR	Contrast-to-Noise Ratio
ECG	Electrocardiogram
FA	Flip Angle
FOV	Field of View
GEFC	Gradient Echo with Flow Compensation
LAD	Left Anterior Descending coronary artery
LVEDV	Left Ventricular End-Diastolic Volume
LVEF	Left Ventricular Ejection Fraction
LVESV	Left Ventricular End-Systolic Volume
LVFW	anterior Left Ventricular Free Wall
MI	Myocardial Infarction
MPIO	Micrometer-sized Iron Oxide Particles
MRI	Magnetic Resonance Imaging
MSME	Multi-Slice Multi-Echo
ROI	Region of Interest
SEM	Standard Error of Mean
SNR	Signal-to-Noise Ratio
SPIO	Small Superparamagnetic Iron Oxide Particles
TE	Echo Time
TR	Repetition Time
USPIO	Ultra-small Superparamagnetic Iron Oxide Particles

SUMMARY

In cellular MRI, micrometer-sized iron oxide particles (MPIO) are a more sensitive contrast agent for tracking inflammatory-cell migration compared to ultra-small superparamagnetic iron oxide particles (USPIO). Inflammation, which promotes adverse tissue remodeling, is known to occur in the viable myocardium adjacent to the necrosed area after a myocardial infarction (MI). This study investigated the temporal relationship between inflammatory cell infiltration and cardiac function during tissue remodeling post-MI using MPIO-enhanced MRI. The MPIO were injected into 7 C57Bl/6 mice (MI+MPIO group) via intravenous administration. The MI was induced 7 days post-MPIO injection. As control groups, 7 mice (Sham+MPIO group) underwent sham-operated surgery without myocardial injury post-MPIO injection and another 6 mice (MI-MPIO group) underwent MI surgery without MPIO injection. MRIs performed post-MI showed a significant signal attenuation at the MI zone in the MI+MPIO group compared to the control groups. The findings suggested that the inflammatory cells containing MPIO infiltrated into the myocardial injury site. Cardiac function was also measured and correlated with the labeled-cell infiltration at the MI site. This study demonstrated a noninvasive technique for monitoring inflammatory cell migration using the MPIO contrast agent. This MPIO-enhanced MRI technique could provide additional insight concerning cardiac disease progression that would improve therapeutic treatment for MI patients.

CHAPTER 1

INTRODUCTION

With the advent of novel contrast agents and cell labeling techniques, the potential of using MRI as a noninvasive tool to *in vivo* detect the localization [1, 2], distribution [3-5] and migration [6, 7] of contrast agent labeled cells has recently been widely studied and evaluated. Iron oxide particles, which predominantly cause signal reduction in T_2^*- and T_2-weighted images, have been applied as negative enhanced contrast agents to a variety of animal models in molecular and cellular imaging [8]. Some of them have the potential of translation from preclinical to clinic diagnostic application.

1.1 MRI and Contrast Agents

MRI is now playing an important role in medical imaging. Its power in diagnostic arena of patient care is unquestionable. MRI is a powerful imaging modality primarily because of its advantage in the soft tissue contrast. This advantage has been further consolidated with the advent of all kinds of contrast agents. The other excitement about MRI is its characteristic of relative safety. Being a noninvasive technique, the MRI employs magnetic fields, which is considered safe at a range of up to 3 Tesla, other than any radiation beam or radionuclide to form the basic principles of imaging.

Generally, MRI provides high contrast-to-noise ratio (CNR) on the appropriate T_1-, T_2- or proton density-weighted image. In most cases the contrast is sufficient to distinguish pathological from healthy tissue. However, in the situations that the inherent contrast could not provide enough differentiation, contrast agents can be used to increase the CNR between diseased and healthy tissue. The MR-sensitive contrast agents usually

are categorized as two classes: paramagnetic contrast agents and superparamagnetic contrast agents, as shown in Table 1.1.

Table 1.1: Classification of MRI contrast agents

	Paramagnetic	Superparamagnetic
T_1 Effect	Strong	Weak
T_2 Effect	Weak	Strong
MRI sequence	T_1-weighted	T_2-weighted
Signal intensity	Hyperintensity	Hypointensity
Example	Gd-DTPA	Iron Oxide Particles

DTPA=diethylenetriaminepentaacetic acid

The paramagnetic contrast agents primarily shorten T_1 value of the targeted tissue and hence render a hyperintense area corresponding to the targeted tissue in the T_1-weighted image. Paramagnetic contrast agents are based on metal ions, such as gadolinium (Gd), manganese (Mn) or europium (Eu), that have a large number of unpaired electrons. The most commonly used clinical paramagnetic contrast agent is gadolinium diethylenetriaminepentaacetic acid (Gd-DTPA).

The Superparamagnetic agents are also called ferromagnetic agents, and primarily shorten T_2 and T_2^* values of the targeted tissue. They render a hypointense area corresponding to the tissue with contrast agents accumulation in the T_2- or T_2^*-weighted image. The superparamagnetic contrast agents consist of small magnetic particles containing iron, and are also referred as superparamagnetic iron oxide particles. The superparamagnetic iron oxide particles usually consist of a crystalline core comprising a mixture of Fe_2O_3 and Fe_3O_4, coated in a polymeric matrix such as dextrin. These particles

have a much higher magnetic moment due to the electron spin coupling in the crystal lattice. They are able to cause inhomogeneity in the local magnetic field and therefore render a shorter T_2^* value.

1.2 Iron Oxide Particles

Iron oxide particles, which predominantly cause signal reduction in T_2^*- and T_2-weighted images as mentioned above, have been applied as negative enhanced contrast agents to a variety of animal models in molecular and cellular imaging [9]. The applications employing iron oxide particles as MRI contrast agent include detection of liver tumors [10-12], lymph node metastases [13-15], inflammatory and degenerative diseases associated with high macrophage activity [16-18]. Several distinct classes of iron oxide particles have widely been used [19] and categorized by size mainly as micrometer-sized iron oxide particles (MPIO, with micrometer diameter) [20-24], small superparamagnetic iron oxide particles (SPIO, with hundreds of nanometer diameter) [25-27] and ultra-small superparamagnetic iron oxide particles (USPIO, with tens of nanometer diameter) [28-31]. In some cases monocrystalline iron oxide nanoparticles (MION) are also used. Two iron oxide compounds have been commercialized for intravenous use: Ferumoxides and Ferucarbotran, both with liver tumors as the clinical targets. Ferumoxides are coated with dextran and Ferucarbotran with carboxydextran.

The iron oxide particles are readily taken up by macrophages [32], which results in their accumulation in the macrophage-rich organs such as liver, spleen, bone marrow and lymphatic nodes [33, 34] following injection. The physicochemical characteristics of the iron oxide particles such as the size, charge, coating, etc, not only affect their imaging efficacy in MRI but also their blood pool kinetics, biodistribution and metabolism in the

applied subjects [8, 35, 36]. The blood half-lives for iron oxide particles are dose dependent and also relate to a progressive saturation of macrophage uptake by the liver or other macrophage-rich organs. For example, the blood half-life of ferumoxtran-10 is 2 to 3 hours in rat and 24 to 36 hours in human at doses of 30 or 45 μmol Fe/kg body weight.

Although the iron oxide uptake by macrophages is well approved by both the *in vitro* and *in vivo* studies, the pathways of transporting iron oxide particles to the local macrophages in the targeted tissue are not clearly defined. There are several pathways potentially existing [16, 37, 38]. The microspheres could be endocytosed by activated blood monocytes which migrate into pathological tissues. They could also be transcytosed across the endothelium by *in situ* macrophages followed by progressive endocytosis. Furthermore, they could be transported into the pathological tissue via the inflammatory neovasculature, with both aforementioned mechanisms involved simultaneously.

One of the common and important applications in iron oxide contrast agents-enhanced MRI is to examine the inflammation process in which macrophages play an important role. Macrophages are able to phagocytose iron oxide particles and home to the disease site. Consequently the iron oxide particle-laden macrophages could be detected and monitored temporally by MRI during the inflammation process. For instance, the iron oxide particles have been used to detect ischemia-associated inflammation [38-41], macrophage-rich atherosclerosis [17, 42, 43], and acute cardiac graft rejection [44, 45]. Recently, MPIO have been studied to evaluate their potential for magnetic resonance cellular imaging and have shown significant promise [32].

The size difference among iron oxide particles can lead to significant differences in their abilities to alter the T_2 relaxation rate R_2. T_1 and T_2 relaxation rate (R_1 and R_2) are defined as the inverse of T_1 and T_2 relaxation time ($R_1 = 1/T_1$ and $R_2 = 1/T_2$), respectively. Furthermore, it can also cause a very different plasma half-life and biodistribution in the subject.

As the study performed in 1.0% agarose gel at 0.47 T over a range of 0-1.0 mM Fe by Williams et al [32], the relaxation rate R_2 of MPIO exhibits a concentration dependency as high as 82.8 $second^{-1}mM^{-1}$, which is much higher than that of USPIO. Furthermore, for MPIO, there was little or no dependency of T_1 relaxation rate on iron content in the preparation (1.2 $second^{-1}mM^{-1}$). This property of MPIO provides advantage over USPIO in largely reducing the T_2 relaxation time without mixing much T_1 effect.

When it comes to the cell labeling and cellular imaging, MPIO labeling can cause greater signal attenuation than smaller particle labeling. Considering the large iron content of MPIO, fewer particles are necessary for sufficient signal attenuation in order to track the labeled cells. It was demonstrated that single cells loaded with single MPIO can be detected [46]. In contrast, accumulation of a considerable number of USPIO in one cell was required to achieve sufficient image contrast [47, 48]. Furthermore, the cell division will dilute the USPIO concentration in the daughter cells and lead to the loss of cell tracking. The MPIO overcome the dilution effect in cell tracking because single MPIO could cause enough signal attenuation. At last, MPIO also render a fast blood pool clearance following the intravenous injection than USPIO, which can potentially shorten the time interval between the injection and the following MRI scanning. The great MR-

sensitivity of MPIO opens up possibilities for *in vivo* tracking of MPIO labeled cells. To date, however, none of the MPIO has been approved by FDA.

As mentioned above, a large portion of iron oxide particles could be taken up by inflammatory cells following injection. In the *in vitro* study also performed by Williams et al [32, 49], it was shown that macrophage has the higher labeling efficiency than other cell types, and that larger particles performing greater labeling efficiency than smaller ones. Table 1.2 shows the percent uptake of MPIO by immune cell types.

Table 1.2: Percent uptake of MPIO by immune cell types

MPIO size	% T cells	% B cells	% Macrophages	% Splenocytes
0.35 μm	3.2	21.2	54	18
0.90 μm	2.8	9.3	73	16.6
1.63 μm	2.7	38.5	72	37

The measurement was determined by fluorescence spectroscopy 24 hours after cell culture. From John B. Williams, et al. (2007)

1.3 Inflammatory Response and Myocardial Infarction

Cardiovascular disease remains the leading cause of death in developed countries, despite recent improvements due to advances in prevention, early diagnosis, and therapeutic and surgical interventions. Experimental evidence strongly supports the conclusion that inflammatory responses, accompanied by elevated levels of cytokines, are a common immunopathological feature following myocardial infarction. These features may contribute to myocardial remodeling and functional outcome for the more than 7.2 million American adults. Triggers of cytokine release in the post-myocardial infarction or ischemic-reperfusion phase include mechanical deformation, reactive oxygen species,

and cytokine feedback amplification pathways. These factors lead to inflammatory cell infiltration into the injured site which, in conjunction with hypo-perfusion due to low blood pressure and poor cardiac output sequelae, produces a positive feedback of the damaging responses. In spite of the established importance of inflammatory cell infiltration into the heart both prior to, and following, myocardial infarction, non-invasive monitoring strategies to assess localized inflammation in affected cardiac tissues are currently extremely limited. Consequently, improvements in imaging techniques to visualize cellular infiltration would greatly advance monitoring of therapeutic effects relevant to both prevention and treatment of cardiovascular diseases.

The findings in the cellular or molecular level provided by contrast agent enhanced MRI techniques also potentially supply an exciting platform to acquire better understanding of the cellular and molecular mechanisms of regulating the inflammatory response following myocardial injuries such as ischemia or infarction [50-52]. Based on the novel understanding, new strategies could be explored to reduce the deleterious remodeling following a MI by promoting effective cardiac tissue repair in cardiology. It is suggested that monocyte-derived macrophages and mast cells may produce cytokines and growth factors necessary for fibroblast proliferation and neovascularization leading to effective repair and scar formation [50]. Despite of the arguments that augmented macrophage homing and inflammatory cytokine production may lead to maladaptive left ventricular remodeling and functional deterioration following a MI [53], Leor and coworkers [54] showed improved scar thickening and cardiac performance. This was demonstrated by injecting human activated macrophages into the ischemic myocardium of rats immediately after coronary artery ligation.

1.4 Research Objects

It is critical to non-invasively evaluate pathophysiological changes in cardiovascular tissues so that prevention and treatment strategies can be implemented as early as possible. The early treatment can minimize or reverse damage after an infarct. The hypothesis for the research is that myocardial injury and cellular infiltration due to inflammatory processes can be quantified non-invasively and that myocardial deficits due to injury and development of inflammatory cell infiltration can be accurately monitored. Based on the hypothesis, the objectives of this research project include developing methods for non-invasive monitoring of inflammatory cell infiltration after myocardial infarction in a murine model. Furthermore, the myocardial remodeling process was monitored by calculating the cardiac function and correlated with the cellular infiltration.

First we injected the MPIO systemically into the mice and waited until the MPIO clearance from the blood pool occurred. A MI was then induced and the potential of MPIO-laden inflammatory cells being activated migrating and homing to the myocardial injury site was examined. The temporal response of MPIO-laden inflammatory cell infiltration into the MI site, as well as cardiac performance was assessed. Provided that the cell mobilization due to myocardial injury could be visualized with appropriate MRI technique, this study will shed light on the investigation of the temporal relationship between the myocardial inflammation and cardiac remodeling progression during the process of a MI.

CHAPTER 2

METHODOLOGY

2.1 Animal Preparation

Adult male C57Bl/6 mice (23.8±1.4 g; 6–11 weeks old) were used following the guidelines of the Animal Care and Use Committee and the Animal Health and Care Section of the Institute (Medical College of Georgia, Augusta, GA, USA). The animals were anesthetized with a mixture of medical air, oxygen (1:1), and 2.0% isoflurane (Abbott Laboratories, Abbott Park, IL, USA), positioned prone upon the animal cradle and maintained at 1.8±0.2% isoflurane level throughout MRI sessions. This protocol maintained a relatively constant respiration rate of 63±6 breaths per minute and heart rate of 437±58 beats per minute during the MRI experiment.

In this study, the animals were divided into three experimental groups: 1) myocardial infarction group with MPIO injection (MI+MPIO, n = 7); 2) myocardial infarction group without MPIO injection (MI-MPIO, n = 6); 3) sham-operated group with MPIO injection (Sham+MPIO, n = 7). For the MI+MPIO and Sham+MPIO groups, the animals were *de novo* labeled via intravenous administration of Bangs particles (Bangs Laboratories, Inc., Fishers, IN, USA), a type of MPIO, at a dose of 0.04 mg Fe/g body weight. At 7 days post- MPIO injection, the MI+MPIO group underwent MI surgery via permanent ligation of the LAD while the Sham+MPIO group underwent open-chest operation without myocardial injury. This study was designed to investigate MPIO-labeled inflammatory cells, predominately macrophages, migrating to the injured site post MI. Therefore for the two groups with MPIO injection the surgery was not performed until the free MPIO were

cleared out from the blood pool. This protocol reduced the possibility of cells that have been directly labeled in the blood pool migrating to the injury site or the local inflammatory cells in the heart endocytosing the circulating MPIO from the blood pool. The 7-day interval between the MPIO injection and surgery allows the particles to be cleared from the blood pool under the detectable level, minimizing potential signal reduction contribution from the blood pool.

2.2 Contrast Agent

The MPIO used in this study are Bangs particles with 1.63 μm diameter. They have a magnetite core (42.5% weight) coated with a polymer. They also carry a Suncoast Yellow fluorescence label with a wavelength of excitation:emission = 540:600 nm.

2.3 Blood Pool Measurement

A blood pool study was performed to evaluate the MPIO blood pool kinetics. This aspect of the overall investigation was performed on 7 additional non-injured animals (25.3±3.4 g; 6-12 weeks old). Blood samples were obtained at various time points post-MPIO injection and MPIO fluorescence intensity measured on a 2-D IVIS 100 Imaging System (Caliper Life Sciences, Hopkinton, MA, USA). One or two blood samples were taken from each mouse once respirations had stabilized after anesthetizing each animal with 1.0% isoflurane. First, a 27-gauge needle, 1-ml syringe and 0.5-ml tube were moistened with Heparin. Then 100 μl of blood was removed by puncturing the needle into the left ventricle of the heart. A 50 μl blood sample was then placed into the 96-well plate for fluorescence imaging.

2.4 Myocardial Infarction Model

Animals were anesthetized with an intraperitoneal ketamine/xylazine cocktail and placed in a supine position. A midline cervical incision was made to intubate the trachea. The intubated mice were connected to a rodent ventilator (CWE Inc., Ardmore, PA, USA) and were ventilated at a respiratory rate of 90 breaths per minute. The chest was opened by middle thoracotomy at the upper sternum, between the fourth and fifth ribs. In the myocardial infarction study, myocardial infarcts were produced by permanently ligating the LAD. The LAD was ligated at a position approximate 1 mm below the left auricle with an 8-0 polypropylene monofilament suture (Ethicon Inc., Somerville, NJ, USA). This induced a detectable area of ischemia in the left ventricle. When the suture was tied, the heart turned pale and an arrhythmia was noted. The sham group underwent chest-open procedures without ligation of the LAD. After surgery the mice were allowed to recover in a recovery chamber at 38 ºC.

2.5 MRI

MRI was performed 1 day before surgery as a baseline, and at 3 (D3), 7 (D7) and 14 days (D14) post-surgery. Images were acquired on a horizontal 7.0-T, 21-cm MRI spectrometer (Bruker Instruments, Billerica, MA, USA) equipped with a micro-imaging gradient insert (950 mT/m). A 35mm inner diameter volume coil was used to transmit and receive signal at ^{1}H frequency (300 MHz). ECG and respiratory signals were monitored and used for gating with a physiological monitoring system (SA Instruments, Inc., Stony Brook, NY). Short-axis images were acquired through the left ventricle and perpendicular to the long axis of the heart using three pulse sequences: (1) A Gradient Echo sequence with Flow Compensation (GEFC) was performed to acquire the T_2^*-weighted images on which signal-to-noise ratio (SNR) and CNR were calculated; (2) A

GEFC cine sequence was performed to acquire the movie of cardiac movement, by which cardiac indices were calculated to evaluate the cardiac function; (3) A Multiple Slices Multiple Echoes (MSME T_2 map) sequence was performed to get the T_2-weighted image and T_2 map. The imaging parameters for the GEFC were: Echo time/Repetition time (TE/TR) = 4/120 ms; flip angle (FA) = 30^o; Field of view (FOV) = 30 x 30 mm; Slice thickness = 1 mm; Matrix = 256 x 256 and 8 averages. The parameters for GEFC cine sequence were: TE/TR = 4/16 ms; FA = 25^o; FOV = 30 x 30 mm; Slice thickness = 1 mm; Matrix = 128 x 128; 8 frames in one cardiac cycle and 8 averages. The parameters for MSME T2 map was: TR = 1000 ms; Average TE = 20 ms with 5 echoes in the echo train; FA = 180^o; FOV = 30 x 30 mm; Slice thickness = 1 mm; Matrix = 256 x 256 and 4 averages. All the three pulse sequences were gated by the ECG signal on the falling edge of the R-wave at the end-diastole, with the T_2 map sequence additionally gated by the respiratory signal.

2.6 Fluorescence Imaging

After the terminal MRI session, the mice were sacrificed and perfused with 4% PFA. Then the heart was removed and fluorescently imaged on the same 2-D IVIS 100 Imaging System used for the blood pool measurement. The MPIO have an outer coating of Suncoast Yellow fluorescence label with a wavelength of excitation:emission = 540:600 nm. The wavelength used to acquire the fluorescence images was Excitation:Emission = 500-550:575-650 nm for the primary image and Excitation:Emission = 460-490:575-650 nm for the background image. The corrected image was obtained by subtracting the background image from the primary image. The imaging parameters for the primary image were: exposure time = 1 second; binning = 2;

f/stop = 2; FOV = 5 cm and subject height = 1.5 cm. Immediately after removal from the animal the heart was placed on the stage inside the imaging chamber with infarction site facing upwards. To ensure that the MPIO injection was successful, *in vivo* fluorescent imaging of the mice liver and spleen was performed immediately after Bangs injection. The rapid Bangs accumulation in the liver and spleen resulted in a strong fluorescent signal. The mouse was shaved and positioned supine on the imaging stage in order to acquire the signal from the liver and spleen. The imaging setup was as follow: exposure time = 1 second; binning = 2; f/stop = 2; FOV = 12.5 cm; and subject height = 1.5 cm.

2.7 Histology

Following fluorescent imaging the heart underwent PFA fixation. After PFA fixation, the heart was cut into sections for staining and histological analysis. Hematoxylin and Eosin (H&E) staining was performed to examine the tissue integrity, F4/80 staining to monitor the inflammatory cells migrating into myocardium, and Prussian Blue staining to detect the existence of iron oxide particles taken up by macrophages.

2.8 Image Processing

Cardiac performance was evaluated using the left ventricular ejection fraction (LVEF). The LVEF was calculated through left ventricular end-diastolic volume (LVEDV) and left ventricular end-systolic volume (LVESV), which were determined from the endocardial contours at the end-diastole and end-systole phase respectively. The regions of interest (ROIs) for calculation were drawn on the continuous short-axis image slices from the apex to the base covering the entire heart.

$$LVEF = \frac{LVEDV - LVESV}{LVEDV} \times 100\% \qquad \text{Equation 1}$$

Signal intensity (SI) and contrast-to-noise ratio (CNR) analysis was performed on GEFC short axis images using Paravision 4.0.1 software (Bruker Instruments, Billerica, MA, USA). Five ROIs, ROI_{MI}, ROI_{adj}, ROI_{ref}, ROI_{sep} and ROI_{bkg}, were delineated to calculate the normalized SI and CNR on the GEFC T_2^*-weighted images. ROI_{MI} was defined as the myocardial infarction region with wall thinning, corresponding to the area with akinetic contractility on the cine images. ROI_{adj} was designated at the area adjacent to the MI site in the left ventricular free wall (LVFW). ROI_{ref} was the reference designated at a relatively clean region remote to the MI site in the intact LVFW. ROI_{sep} was designated in the interventricular septum close to the MI site. ROI_{bkg} was placed on the background to calculate the signal intensity of the background noise. CNR between the myocardial infarction region ROI_{MI} and the reference ROI_{ref} was defined through Equation 2:

$$CNR_{MI} = \frac{SI_{MI} - SI_{ref}}{SI_{bkg}} \qquad \text{Equation 2}$$

SI_{MI}, SI_{ref} and SI_{bkg} were the mean signal intensity of ROI_{MI}, ROI_{ref} and ROI_{bkg} respectively. The signal intensity was normalized to the reference area, with the normalized signal intensity of the adjacent area, septum, and MI site defined as follows:

$$SI_{adj}^{norm} = \frac{SI_{adj}}{SI_{ref}} \qquad \text{Equation 3}$$

$$SI_{sep}^{norm} = \frac{SI_{sep}}{SI_{ref}} \qquad \text{Equation 4}$$

$$SI_{MI}^{norm} = \frac{SI_{MI}}{SI_{ref}}$$ Equation 5

SI_{adj} and SI_{sep} were the mean signal intensity of ROI_{adj} and ROI_{sep} respectively.

2.9 Statistical Analysis

All data was presented as mean ± standard error of mean (SEM). To compare the difference of CNR values and LVEF values among the three experimental groups, two-way repeated-measures ANOVA was used, followed by Bonferroni post-hoc test to specially compare two assigned groups. A linear regression was used to determine if a correlation existed between the inflammatory-cell infiltration represented by the CNR at the MI site and cardiac remodeling represented by the LVEF. The first order exponential curve fitting was used to estimate the half life of MPIO washout in the blood pool. The GraphPad Prism 5.01 (GraphPad Software Inc., San Diego, CA, USA) was used for all statistical analyses.

CHAPTER 3

RESULTS

3.1 Blood Pool Kinetics

It is critical to understand the blood pool kinetics of the MPIO in order to determine the proper timing to introduce an experimental myocardial infarction without having residual effects of the negative MRI enhancement from the circulating particles. Based on the optical imaging data shown in Figure 1, the signal intensity for the blood samples reaches a maximum within 30 seconds post-MPIO injection. Furthermore, MPIO was quickly washed out from the blood pool as the half life was less than 1 minute (T = 0.73 minutes; $r^2 = 0.94$). Therefore, the 7-day interval between MPIO injection and MI was sufficient for allowing particles to clear from the blood pool, which minimized signal attenuation caused by particles otherwise remaining in the peripheral blood pool. In this manner, inflammatory cells mobilizing to the myocardial injury by remote recruitment were distinguished from the resident inflammation-activated immune cells.

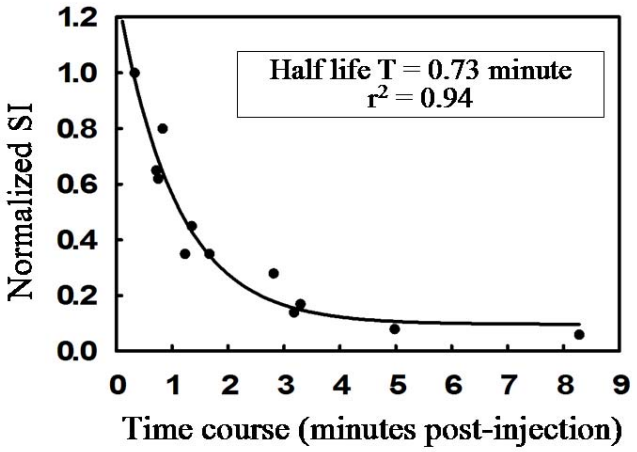

Figure 1: MPIO washout in blood

3.2 MPIO-Labeled Inflammatory Cell Infiltration

Both T_2*-weighted images and T_2 map were acquired and used for analysis to determine the extent to which infiltration of inflammatory cells into the MI site could be monitored using MPIO-enhanced MRI. As shown in Figure 2, gradual signal attenuation at the MI site was observed in the MI+MPIO group post-surgery. No detectable signal attenuation was observed at the corresponding site in either MI-MPIO or Sham+MPIO group. There was no significant difference at the corresponding site between the pre- and post-surgery images in all the groups. In order to prove that the pronounced signal attenuation around the MI site was caused by the infiltration of MPIO-laden inflammatory cells, the MRI findings were further validated with fluorescence imaging and histology.

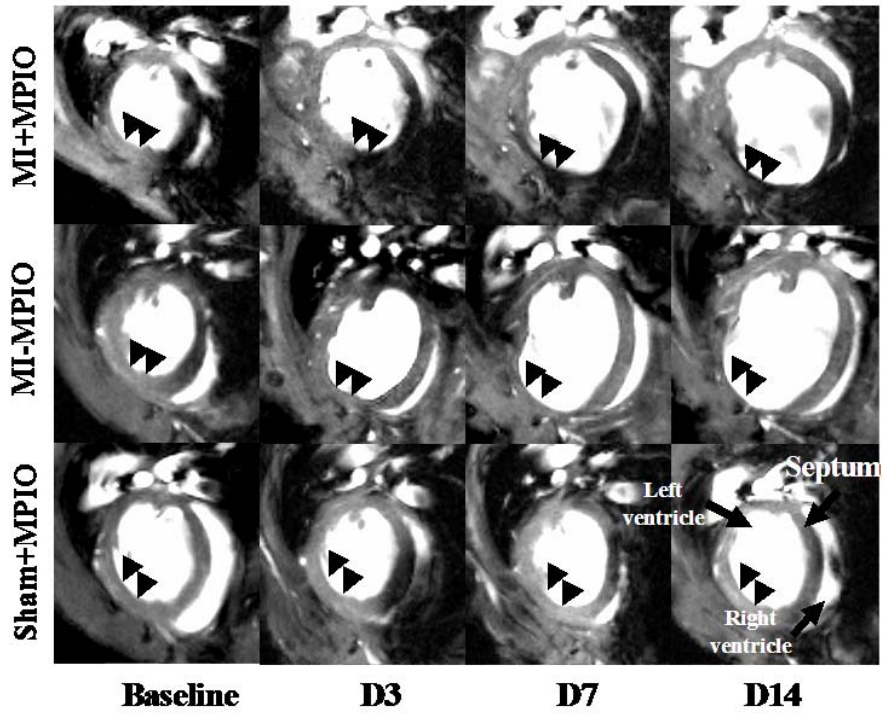

Figure 2: Longitudinal MRI. The T_2^*-weighted images were acquired at baseline, 3, 7 and 14 days post-surgery. The image at bottom right shows the cardiac geometry.

To demonstrate that the pronounced signal attenuation around the MI site was caused by infiltration of MPIO-laden inflammatory cells, the MRI findings were correlated with histology and fluorescence imaging. Figure 3 A and B are the montage heart slices by macroscopic images with 10x magnification from a representative MI+MPIO heart and a Sham+MPIO heart respectively. In Figure 3A, a considerable number of MPIO-labeled cells were localized at the MI and adjacent area as indicated by the arrows, while no MPIO-labeled cells were observed in the sham heart in Figure 3B. Comparison between the Prussian blue staining and MRI demonstrated the co-registered MPIO distribution. The hypo-intense area in the T_2*-weighted image and area with dark spots in the T_2 map co-localized well with each other and also with the iron accumulation in the Prussian blue staining. For the MI+MPIO group, as shown in Figure 3 C and D, the histology showed the co-localization of the Prussian blue and F4/80 staining, indicating that an appreciable amount of iron was incorporated in the macrophages. For the Sham+MPIO group, as shown in Figure 3 F and G, no F4/80 or Prussian blue positive cell was observed. For the MI-MPIO group, there were a considerable number of F4/80 positive macrophages around the MI site, while no Prussian blue stained cells were co-localized with them. It was observed a very small amount of iron scattered around the LVFW in the MI-MPIO group, which might be caused by the hemorrhage during the MI surgery. In the *ex vivo* fluorescent image shown in Figure 3 E and H, a strong signal observed at the MI region in the representative MI+MPIO heart (Figure 3E) indicated localized Bangs particles, while the Sham+MPIO heart (Figure 3H) lacked fluorescence signal enhancement. The current results imply that a considerable quantity of macrophages labeled with MPIO can

potentially mobilize, infiltrate, and engraft into the myocardial injury site and cause significant signal attenuation in MRI T_2*-weighted and T_2-weighted images.

In this study, normalized signal intensity at the septum, MI site and the adjacent area, and CNR at the MI site were calculated and analyzed to quantify the infiltration of

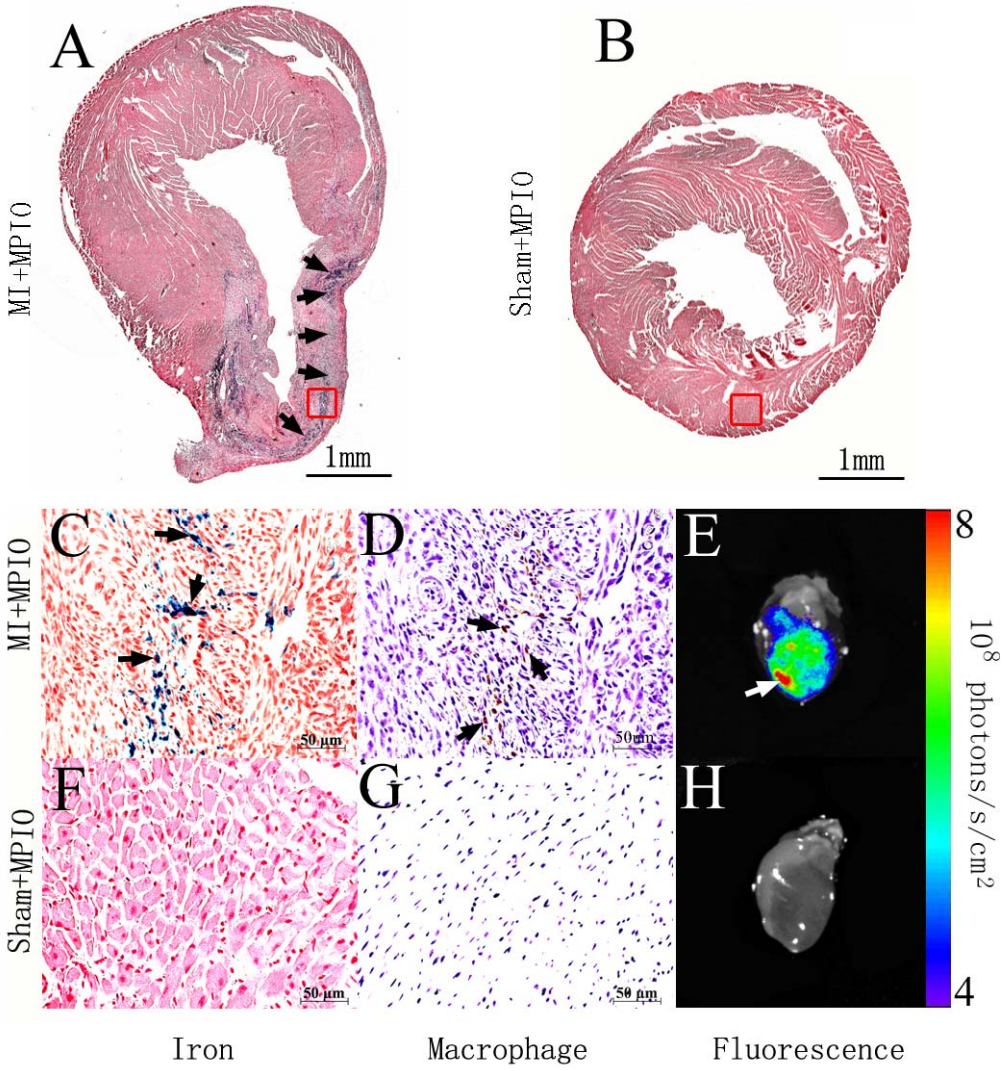

Figure 3: Histology images. The MI and Sham hearts were excised 7 days post-surgery. The images A and B show the whole heart slices montaged with about 30 macroscopic images (10x magnification). C and D are corresponding to the enlargement of the area boxed with the red lines in image A, and F and G to that in image B. C and F are Prussian blue staining for iron, D and G are F4/80 staining for macrophages, and E and H are fluorescent images of the whole hearts.

MPIO-labeled inflammatory cells following myocardial injury. The definition for normalized signal intensity and CNR can be found in Section 2.8 equation 2-5.

To evaluate the temporal variation of normalized signal intensity of various zones, the SNRs of different ROIs were calculated and then normalized to the SNR of the reference, which gives the results of equation 3 to 5 in Section 2.8. In the Sham+MPIO group, a false MI zone was designated in the region corresponding to that of the MI groups assuming existence of a MI site. As shown in Figure 4, the MI+MPIO group demonstrate gradual signal attenuation at the MI site. The signal intensity dropped dramatically within one week post-MI and did not show much change between D7 and D14. The normalized signal intensity at the corresponding site in the two control groups did not change significantly over the experiment duration. For the normalized signal intensity at the adjacent zone, no signal attenuation was observed in the Sham+MPIO group, and little attenuation was observed in the two MI groups. This attenuation in the two MI groups may be due to the necrosis of the myocardium near the suture or the hemorrhage during the MI surgery, which could result in blood iron leakage. For the normalized signal intensity at the septum, it shows greater attenuation in the two MPIO injected groups (MI+MPIO and Sham+MPIO) than in the MI-MPIO group. There was an obvious trend of gradual signal attenuation at the MI site, but no significant attenuation trend was observed at the adjacent zone or septum for the MI+MPIO group. This suggests that MPIO-laden inflammatory cells (mainly macrophages) mobilize and infiltrate to the MI site gradually, and can be monitored by MRI temporally.

For the CNR analysis and comparison, as shown in the Table 3.1, the CNR post-surgery was significantly different between the MI+MPIO and the other two control

groups. The negative CNR values indicate a hypo-intensity at the MI zone. The more negative the CNR, the more attenuated the signal was at the MI zone relative to that in the healthy myocardium, and hence it indicated more MPIO-labeled inflammatory cell infiltration. The temporal characteristics of the CNR had a similar attenuation trend with that of the normalized signal intensity at the MI site. The CNR, which shows the difference between the MI zone and the reference, not only indicates the global mobilization and infiltration of MPIO-laden inflammatory cells into the MI site, but could also indicate the redistribution of the MPIO-laden inflammatory cells between the reference area and the MI site. Since the relatively stable signal intensity at the reference area was observed over the experiment duration, the later possibility of redistribution is eliminated. Hence the normalized signal intensity and CNR data at the MI site suggests a global inflammatory cell migration and infiltration following the myocardial infarction.

Table 3.1: Contrast-to-noise ratio values

Time	MI + MPIO (n = 7)	Sham + MPIO (n = 7)	MI - MPIO (n = 6)
Baseline	0.40 ± 1.03	-0.07 ± 0.5	0.16 ± 0.99
Day 3 post-surgery	-6.80 ± 1.38	-0.88 ± 1.16 **	-1.84 ± 1.35 #
Day 7 post-surgery	-8.80 ± 1.14	0.65 ± 0.84 **	-1.86 ± 1.22 ##
Day 14 post-surgery	-9.98 ± 0.97	-0.12 ± 0.43 **	-3.10 ± 1.03 ##

Note: Values are mean ± SEM.
* denotes comparison between MI + MPIO and Sham + MPIO group; p(**)< 0.001.
# denotes comparison between MI + MPIO and MI – MPIO group; p(#)<0.01 and p(##)<0.001.

3.3 Temporal Features of Cardiac Remodeling

LVEF, LVEDV, and LVESV were used to evaluate the cardiac performance and remodeling process post-surgery. As shown in Figure 5, LVEDV and LVESV increased markedly post-MI in the two MI groups, but with obviously different rates at different time intervals, determined by the slopes of the curve. The most dramatic change in cardiac function took place within 1 week post-MI, which potentially reflected a fast left ventricular remodeling process. After 7 days post-MI, the increase of both LVEDV and LVESV slowed down, which is reflected from the smaller curve slopes. The LVEF declined within one week post-MI, and gradually became stabilized afterwards. The cardiac function for the sham group did not change much and stayed normal over the experiment duration. The LVEF values are shown in Table 3.2. Two-way repeated-measures ANOVA showed a significant difference among the 3 treatments ($p<0.0001$), and significant differences were also obtained between the sham and two MI groups at all the time points post-surgery ($p<0.001$) using Bonferroni post-hoc test. The information from the cardiac indices is important and necessary to monitor the cardiac performance and remodeling progression, especially when investigating changes during disease progression. The experimental data also indicates the consistence of using MRI as a tool to monitor the cardiac function.

3.4 Correlation of Inflammatory Cell Infiltration and Cardiac Remodeling

To examine the temporal relationship between the cardiac remodeling and the infiltration progression of the MPIO-laden inflammatory cells, a linear regression was used. The infiltration was represented by the CNR at the MI site, and the cardiac remodeling by the LVEF. The temporal MPIO-labeled inflammatory cell infiltration would lead to the gradual CNR attenuation at the MI site. The linear regression was to

test the extent to which CNR was correlated to the LVEF. The LVEF and CNR at the MI site had similar characteristics of time dependence over the experimental time course (Figure 6). Both had rapid attenuation within one week following MI, before a reduction in the rate of attenuation. The correlation was examined by the linear regression of CNR versus LVEF, as shown in Figure 6. The result indicates a positive linear correlation (r^2=0.98, slope=0.332) and suggests that the inflammatory cell infiltration post-MI was associated with the remodeling progression.

Table 3.2: Left ventricular ejection fraction values

Time	MI + MPIO (n = 7)	Sham + MPIO (n = 7)	MI - MPIO (n = 6)
Baseline	69.85 ± 2.46%	71.61 ± 0.81%	69.34 ± 2.78%
Day 3 post-surgery	49.68 ± 3.50% **	72.27 ± 0.25%	51.26 ± 4.01% ##
Day 7 post-surgery	40.50 ± 4.91% **	73.57 ± 1.43%	38.09 ± 2.55% ##
Day 14 post-surgery	40.08 ± 5.29% **	73.87 ± 2.26%	43.42 ± 3.77% ##

Note: Values are mean ± SEM.
* denotes comparison between MI + MPIO and Sham + MPIO group; p(**)< 0.001.
# denotes comparison between MI - MPIO and Sham + MPIO group; p(##)<0.001.

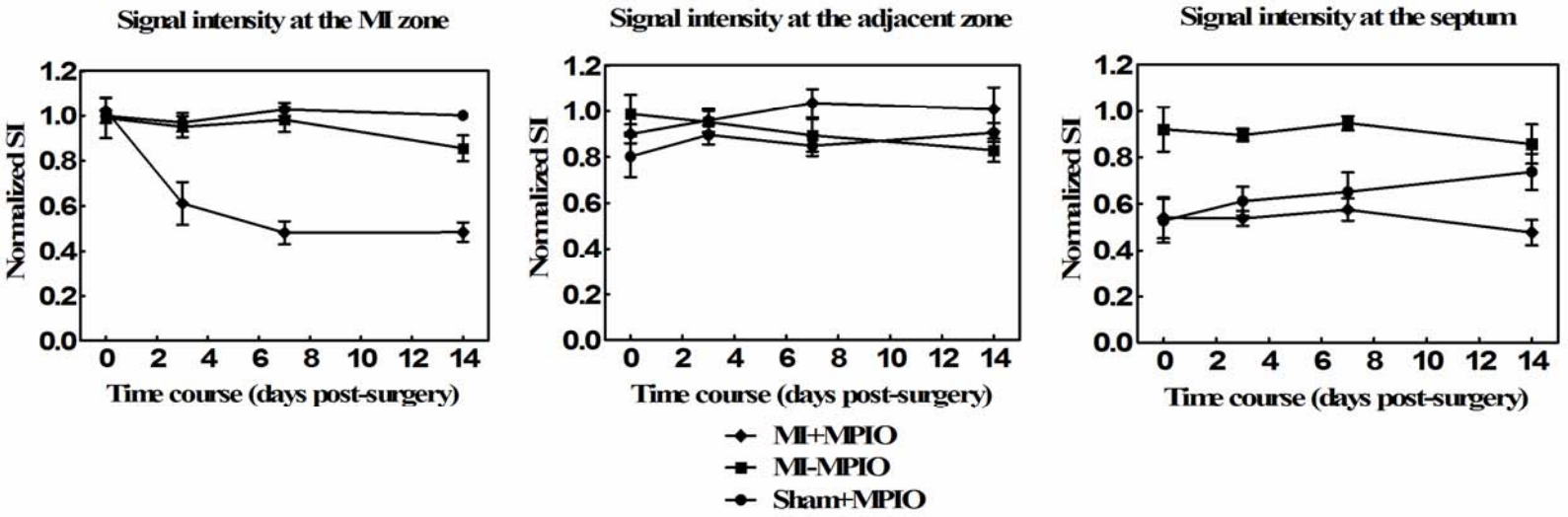

Figure 4: Normalized signal intensity at various zones. The MRI signal intensity was normalized to that at a reference designated at the healthy myocardium remote to the MI site. The data was presented as mean±SEM.

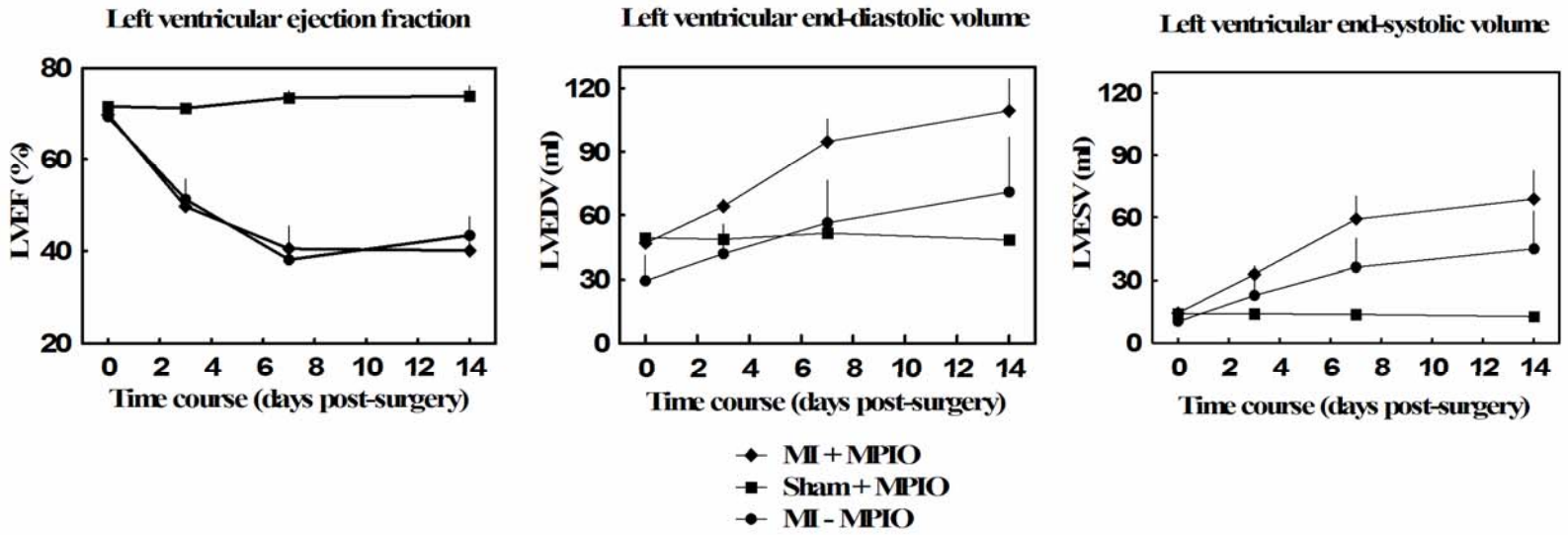

Figure 5: Cardiac function. The data was presented as mean±SEM.

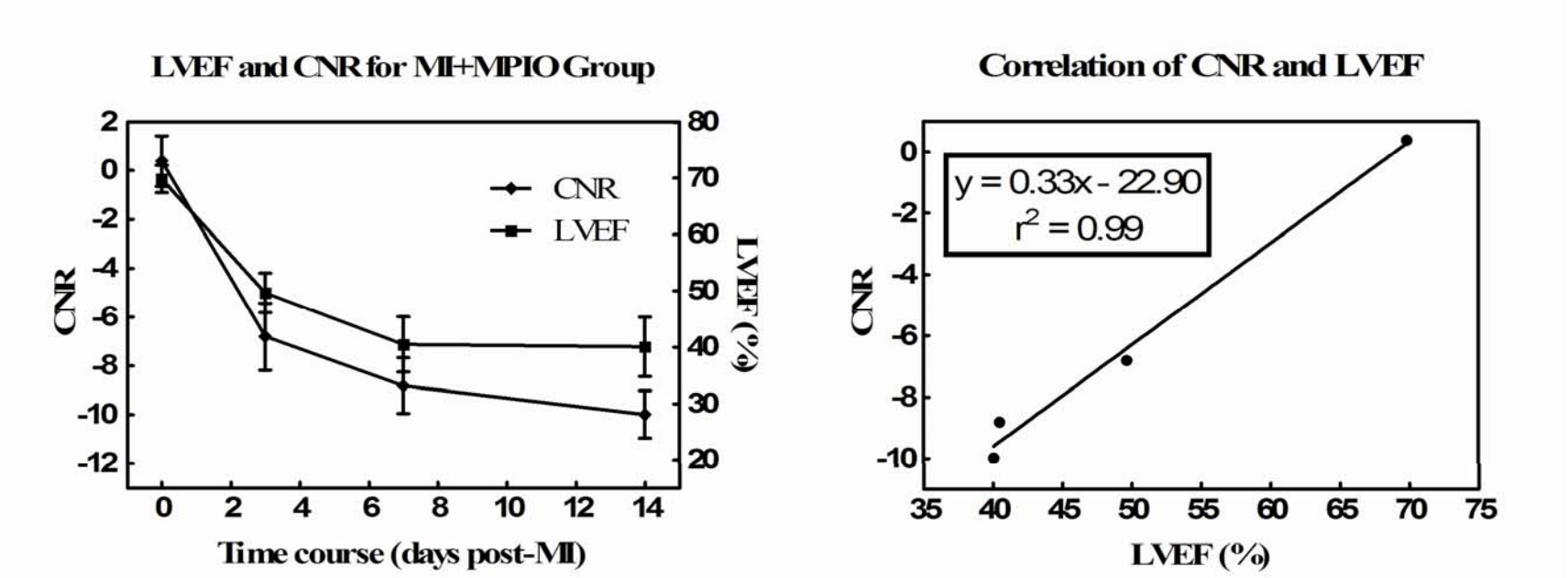

Figure 6: Correlation of CNR and LVEF. The MPIO-labeled inflammatory cell infiltration was represented by CNR at the MI site, and cardiac remodeling by LVEF. On the left, CNR and LVEF were plotted in the same chart. Linear regression on the right demonstrated a positive correlation between them.

CHAPTER 4

DISCUSSION

Unlike other cell types that do not freely incorporate contrast agents without the existence of transfection agents, macrophages readily take up MPIO while keeping their ability to migrate and engraft into the inflammation sites. T cells, B cells and macrophages all have considerable capability of incorporating MPIO. However, the highest incorporation was observed in the culture of macrophages [32]. The characteristic of macrophages taking up MPIO paves the way to monitor and potentially quantify the migration and accumulation of macrophages by noninvasive MRI. It has been approved as an effective method to detect and monitor macrophage infiltration to the myocardial infarction site using iron oxide-enhanced MRI [55].

Following the systemic administration, the iron oxide particles circulating in the blood pool are preferentially phagocytosed by immune cells before clearance within reticuloendothelial system [27]. Iron oxide particles are mainly accumulated in liver, spleen, bone marrow and lymph node [34, 36]. Knowing the clearance rate of the MPIO from the mouse blood pool provides a better understanding as to when the peripheral blood pool ceases to provide significant contrast enhancement and therefore an experimental myocardial infarction should be introduced. However, the half life of MPIO in the blood pool is dose dependent[8]. Hence it is necessary to first acquire the information of blood pool half life at a particular dose before designing a protocol to monitor the MPIO-labeled cell infiltration.

In this study the MRI was performed at three temporal points post-MI within the experimental course. Within one week post-MI, there are dramatic changes for both cardiac performance and inflammatory cell infiltration. The early phase might be important to study the inflammation following a MI. The signal attenuation was relatively steady after one week post-MI. Considering the high dose injected, however, the T_2* effect might be saturated due to the large amount of iron accumulation. As a result, the further infiltration of MPIO-laden cells could not be differentiated at 14 days post-MI. The stabilized signal reduction potentially indicates that the iron was kept in the MI site for an appreciable period. Therefore the experimental design for future studies should include a longer time course in order to acquire information about the later phase of cardiac remodeling and potential washout of the iron from the infarcted heart.

The macrophages are activated by myocardial injury and will recruit free MPIO, if any, directly from the blood pool [8]. In contrast to prior published results in which iron oxide particles were injected post-cardiac injury [55], in our study the MPIO were injected prior to myocardial infarction. The myocardial injury was induced after the clearance of iron oxide particles from the peripheral blood pool. Hence the local activated immune cells in the infarcted heart could not phagocytize the circulating MPIO directly from blood. Following the MI, the MPIO-labeled immune cells, in particular, macrophages would mobilize to the myocardial injury site. We can therefore distinguish the pre-labeled immune cells from the resident activated inflammation-related immune cells. Furthermore, the mobilization and infiltration of pre-labeled immune cells could be tracked temporally during the entire process of the myocardial infarction. Therefore this

pre-labeling technique is potentially a better way to monitor disease progression in a pre-clinic model.

It is advantageous to study the inflammation and the function of inflammatory cells in the process of myocardial infarction by pre-labeling inflammatory cells *de novo* as compared to injecting *in vitro* labeled cells directly into the infarcted heart. In the *in vitro* cell-labeling technique, the functionality of labeled cells might be affected due to the *in vitro* labeling environment. An appreciable number of cells might die during or after the injection process. Furthermore, in the case of cardiac study, the injection directly to the myocardial infarction and adjacent zones has a potential risk to injure the myocardium further and cause irreversible damage. By using the *de novo* labeling method, however, a variety of cell types might take up the iron oxide particles instead of one specific cell type. Hence the potential disadvantage of the current study is the non-specific labeling where it unavoidably affects the specificity of the study in regard to a specific cell type, e.g. macrophages.

To quantify labeled-cell infiltration more accurately in the MRI, novel methods are warranted other than using the SNR and CNR as representative indices. SNR and CNR have intrinsic variation due to the fluctuation of the magnetic resonance spectrometer during the experimental time course and also have dependence on the individual magnetic resonance system and imaging protocol implementation. Furthermore, the SNR and CNR calculated through the mean signal intensity of chosen ROIs, generally represent the density of accumulated iron oxide particles other than any information regarding spread or number of labeled cells over the infarction site. More quantitative methods in which the labeled cells could be counted are potentially better ways.

Moreover, the dose of MPIO warrants further optimization. Excessive dose may lead to MPIO saturation at the MI zone while an insufficient dose may result in an undetectable number of MPIO-laden inflammatory cells, both leading to images with dark spots that may be hard to differentiate.

CHAPTER 5

CONCLUSION

In this experiment, the inflammatory cell migration following myocardial infarction was monitored using non-invasive MRI technique. First, the blood pool kinetics of the MPIO, Bangs, was examined and the half life of the MPIO clearance from the blood pool was estimated. The 7-day interval between the injection of the MPIO and the induction of myocardial infarction allowed for complete clearance of the MPIO from the blood pool, minimizing the signal reduction contribution from the circulating MPIO otherwise remaining in the blood pool.

Second, the infiltration of labeled inflammatory cells into the MI heart was studied. The gradual signal attenuation was observed at the MI site in the MI+MPIO group using MRI. The normalized signal intensity and CNR differences were significant between the MI+MPIO group and the two control groups. The MRI findings were further validated by the fluorescence imaging and histology, in which localized MPIO were indicated and correlated well with the hypo-intense area in the T_2*- and T_2-weighted MRI. Furthermore, histology results indicated considerable numbers of cells localized with Bangs were macrophages. However, other cell types also potentially exist.

Third, the temporal features of left ventricular cardiac function were examined. The decrease of LVEF, increase of LVEDV and LVESV post MI indicated a cardiac remodeling following myocardial infarction. These indices could be important for monitoring the cardiac remodeling in the study of disease progression.

Last, to study the temporal correlation between cardiac remodeling and the MPIO-labeled inflammatory cell infiltration, the linear regression was performed between LVEF and CNR at the MI site. The results showed a positive correlation, which demonstrated that the MPIO-labeled inflammatory cells migrated and engrafted to the MI site with the progression of cardiac remodeling.

Overall, the inflammatory cells migration following MI could be tracked using the MPIO-enhanced MRI technique noninvasively and temporally. Normalized signal intensity and CNR at the MI site could be used as indices to monitor and quantify the infiltration of MPIO-labeled inflammatory cells in murine MI model.

APPENDIX A

RAW DATA

Table A.1: MI+MPIO group LVEF data

Mouse Number	Baseline	D3	D7	D14
MI 1	72.55%	59.14%	56.12%	61.39%
MI 2	65.48%	49.69%	55.22%	55.64%
MI 3	62.43%	42.19%	31.51%	31.30%
MI 4	68.39%	34.36%	24.41%	25.58%
MI 5	68.18%	57.77%	50.26%	34.51%
MI 6	82.80%	47.01%	31.37%	28.03%
MI 7	69.09%	57.60%	34.61%	44.09%
Mean	69.85%	49.68%	40.50%	40.08%
SEM	2.46%	3.50%	4.91%	5.29%

Table A.2: MI-MPIO group LVEF data

Mouse Number	Baseline	D3	D7	D14
MI Control1	NA	56.32%	37.06%	47.64%
MI Control2	64.05%	36.88%	31.83%	28.32%
MI Control3	68.30%	41.35%	32.53%	35.13%
MI Control4	62.16%	52.75%	48.15%	46.43%
MI Control5	80.81%	66.11%	44.50%	56.16%
MI Control6	71.40%	54.16%	34.44%	46.85%
Mean	69.34%	51.26%	38.09%	43.42%
SEM	7.35%	10.60%	6.74%	9.98%

Table A.3: Sham+MPIO group LVEF data

Mouse Number	Baseline	D3	D7	D14
Sham 1	68.23%	71.79%	71.29%	77.81%
Sham 2	70.30%	72.74%	73.87%	75.02%
Sham 3	75.03%	68.54%	75.80%	70.25%
Sham 4	72.53%	72.98%	70.52%	68.42%
Sham 5	71.09%	67.27%	72.65%	70.53%
Sham 6	72.76%	72.38%	80.81%	85.16%
Sham 7	71.34%	72.83%	70.02%	69.91%
Mean	71.61%	72.27%	73.57%	73.87%
SEM	0.81%	0.25%	1.43%	2.26%

Table A.4: MI+MPIO group SNR and CNR data

Mouse Number	Baseline					D3					D7					D14				
	SNR Adj.	SNR MI	SNR Sep.	SNR Ref.	CNR MI	SNR Adj.	SNR MI	SNR Sep.	SNR Ref.	CNR MI	SNR Adj.	SNR MI	SNR Sep.	SNR Ref.	CNR MI	SNR Adj.	SNR MI	SNR Sep.	SNR Ref.	CNR MI
MI 1	15.02	16.24	6.80	15.02	1.22	12.35	9.35	10.01	15.44	-6.09	20.00	6.85	12.75	18.59	-11.74	22.02	10.64	12.76	21.21	-10.56
MI 2	14.16	16.16	8.88	14.16	2.00	17.67	12.67	9.46	15.95	-3.28	12.15	5.66	8.84	13.58	-7.93	14.10	6.08	12.42	17.56	-11.48
MI 3	14.81	14.13	10.34	17.21	-3.07	22.28	19.99	10.20	23.65	-3.66	15.11	9.85	4.79	15.38	-5.53	22.01	9.09	7.42	18.76	-9.67
MI 4	17.37	15.78	5.88	18.11	-2.33	16.90	4.84	8.84	17.36	-12.52	12.05	9.14	8.83	14.78	-5.64	11.02	9.70	6.73	17.17	-7.47
MI 5	14.09	25.13	10.14	20.10	5.03	22.94	13.95	9.92	20.44	-6.49	17.19	8.21	10.11	17.39	-9.17	18.37	9.74	7.37	15.58	-5.84
MI 6	16.95	19.80	5.99	20.30	-0.50	11.68	3.70	9.12	14.79	-11.09	23.55	5.26	10.32	18.94	-13.67	27.23	6.38	9.95	19.70	-13.33
MI 7	22.94	24.56	23.59	24.13	0.43	23.70	19.81	11.38	24.27	-4.46	22.72	10.32	11.89	18.26	-7.94	20.82	13.29	6.81	24.77	-11.48
Mean	16.47	18.83	10.23	18.43	0.40	18.22	12.04	9.85	18.84	-6.80	17.54	7.90	9.65	16.70	-8.80	19.37	9.27	9.07	19.25	-9.98
SEM	1.18	1.68	2.34	1.29	1.03	1.88	2.47	0.32	1.49	1.38	1.79	0.76	0.98	0.80	1.14	2.05	0.94	1.00	1.15	0.97

Table A.5: MI-MPIO group SNR and CNR data

Mouse Number	Baseline					D3					D7					D14				
	SNR Adj.	**SNR MI**	**SNR Sep.**	**SNR Ref.**	**CNR MI**	**SNR Adj.**	**SNR MI**	**SNR Sep.**	**SNR Ref.**	**CNR MI**	**SNR Adj.**	**SNR MI**	**SNR Sep.**	**SNR Ref.**	**CNR MI**	**SNR Adj.**	**SNR MI**	**SNR Sep.**	**SNR Ref.**	**CNR MI**
MI Ctl1	NA	NA	NA	NA	NA	23.85	23.89	18.68	21.28	21.79	22.20	26.56	23.44	24.48	25.55	23.80	26.33	21.48	19.34	28.02
MI Ctl2	37.62	34.51	31.21	34.16	34.61	32.97	34.22	29.16	35.97	32.79	25.98	28.93	31.48	19.94	31.74	16.15	13.12	11.17	24.13	21.38
MI Ctl3	21.26	22.02	18.69	20.83	27.99	26.53	24.73	25.18	24.69	24.74	21.26	22.02	18.69	20.83	18.49	24.44	24.02	22.51	24.65	26.20
MI Ctl4	28.13	30.48	28.78	20.84	23.26	25.33	25.79	26.30	27.23	29.64	16.97	22.87	25.14	27.24	24.48	22.41	21.68	24.66	24.05	23.26
MI Ctl5	13.87	13.79	13.39	6.71	16.46	26.48	26.62	25.28	23.59	30.23	29.25	28.29	24.15	22.19	27.87	17.76	27.49	24.08	22.86	28.43
MI Ctl6	14.34	13.95	13.46	9.21	13.78	30.31	30.30	32.47	25.74	37.36	21.95	22.53	24.16	14.73	28.19	13.81	12.31	17.54	6.25	16.27
Mean	23.05	22.95	21.10	18.35	23.22	27.58	27.59	26.18	26.42	29.43	22.94	25.20	24.51	21.57	26.05	19.73	20.83	20.24	20.22	23.93
SEM	4.48	4.22	3.77	4.90	3.20	1.29	1.49	1.74	1.93	2.11	1.59	1.17	1.55	1.61	1.69	1.67	2.49	1.93	2.69	1.75

Table A.6: Sham+MPIO group SNR and CNR data

Mouse Number	Baseline					D3					D7					D14				
	SNR Adj.	SNR MI	SNR Sep.	SNR Ref.	CNR MI	SNR Adj.	SNR MI	SNR Sep.	SNR Ref.	CNR MI	SNR Adj.	SNR MI	SNR Sep.	SNR Ref.	CNR MI	SNR Adj.	SNR MI	SNR Sep.	SNR Ref.	CNR MI
Sham 1	13.02	13.73	6.18	14.17	-0.44	14.98	19.20	10.23	18.74	0.46	20.84	27.40	15.86	26.37	1.04	17.41	19.52	17.41	19.72	-0.21
Sham 2	12.95	18.61	6.50	19.38	-0.77	24.17	22.10	9.85	26.10	-4.00	25.82	28.16	10.93	30.26	-2.10	22.42	23.52	21.70	21.70	1.82
Sham 3	22.43	22.82	5.38	23.17	-0.34	30.54	26.41	14.33	31.82	-5.41	26.87	28.65	11.55	29.82	-1.17	31.01	34.26	13.92	36.22	-1.96
Sham 4	26.19	29.17	14.54	29.89	-0.72	26.89	27.83	19.19	25.17	2.66	26.99	30.20	22.62	26.01	4.19	30.96	33.93	19.85	33.96	-0.02
Sham 5	25.56	26.81	22.76	28.03	-1.22	27.11	31.10	17.69	29.85	1.26	22.58	26.91	24.42	27.59	-0.68	26.37	30.97	24.53	30.77	0.19
Sham 6	9.69	30.75	14.00	30.56	0.19	21.87	22.61	18.58	25.07	-2.46	23.98	29.95	22.25	27.26	2.68	27.99	25.59	21.62	26.34	-0.76
Sham 7	23.37	27.71	22.89	24.93	2.77	23.09	32.81	25.47	31.48	1.33	21.10	32.42	20.04	31.84	0.59	24.17	32.96	23.14	32.83	0.13
Mean	19.03	24.23	13.18	24.30	-0.07	24.09	26.01	16.48	26.89	-0.88	24.03	29.10	18.24	28.45	0.65	25.76	28.68	20.31	28.79	-0.12
SEM	2.60	2.34	2.86	2.25	0.50	1.87	1.88	2.08	1.74	1.16	0.99	0.72	2.07	0.83	0.84	1.85	2.20	1.37	2.39	0.43

REFERENCES

1. Kawahara I, Nakamoto M, Kitagawa N, Tsutsumi K, Nagata I, Morikawa M, Hayashi T, *Potential of magnetic resonance plaque imaging using superparamagnetic particles of iron oxide for the detection of carotid plaque.* Neurologia Medico-Chirurgica(Tokyo), 2008. **48**(4): p. 157-61; discussion 161-2.

2. Lepore AC, Walczak P, Rao MS, Fischer I, Bulte JWM, *MR imaging of lineage-restricted neural precursors following transplantation into the adult spinal cord.* Experimental Neurology, 2006. **201**(1): p. 49-59.

3. Kim D, Chun BG, Kim YK, Lee YH, Park CS, Jeon I, Cheong C, Hwang TS, Chung H, Gwag BJ, Hong KS, Song J, *In vivo tracking of human mesenchymal stem cells in experimental stroke.* Cell Transplant, 2008. **16**(10): p. 1007-12.

4. Farrell E, Wielopolski P, Pavljasevic P, van Tiel S, Jahr H, Verhaar J, Weinans H, Krestin G, O'Brien FJ, van Osch G, Bernsen M, *Effects of iron oxide incorporation for long term cell tracking on MSC differentiation in vitro and in vivo.* Biochemical and Biophysical Research Communications, 2008. **369**(4): p. 1076-81.

5. Arbab AS, Frank JA, *Cellular MRI and its role in stem cell therapy.* Regenerative Medicine, 2008. **3**(2): p. 199-215.

6. Arbab AS, Janic B, Knight RA, Anderson SA, Pawelczyk E, Rad AM, Read EJ, Pandit SD, Frank JA, *Detection of migration of locally implanted AC133+ stem cells by cellular magnetic resonance imaging with histological findings.* The FASEB Journal: official publication of the Federation of American Societies for Experimental Biology, 2008. **22**(9): p. 3234-46.

7. Jendelová P, Herynek V, Urdzíková L, Glogarová K, Kroupová J, Andersson B, Bryja V, Burian M, Hájek M, Syková E, *Magnetic resonance tracking of transplanted bone marrow and embryonic stem cells labeled by iron oxide nanoparticles in rat brain and spinal cord.* Journal of Neuroscience Research, 2004. **76**(2): p. 232-43.

8. Corot C, Robert P, Idée JM, Port M, *Recent advances in iron oxide nanocrystal technology for medical imaging.* Advanced Drug Delivery Reviews, 2006. **58**(14): p. 1471-504.

9. Burns TC, Ortiz-González XR, Gutiérrez-Pérez M, Keene CD, Sharda R, Demorest ZL, Jiang Y, Nelson-Holte M, Soriano M, Nakagawa Y, Luquin MR, Garcia-Verdugo JM, Prósper F, Low WC, Verfaillie CM, *Thymidine analogs are transferred from prelabeled donor to host cells in the central nervous system after transplantation: a word of caution.* Stem Cells, 2006. **24**(4): p. 1121-7.

10. Bellin MF, Zaim S, Auberton E, Sarfati G, Duron JJ, Khayat D, Grellet J, *Liver metastases: safety and efficacy of detection with superparamagnetic iron oxide in MR imaging.* Radiology, 1994. **193**(3): p. 657-63.

11. Bluemke DA, Weber TM, Rubin D, de Lange EE, Semelka R, Redvanly RD, Chezmar J, Outwater E, Carlos R, Saini S, Holland GA, Mammone JF, Brown JJ, Milestone B, Javitt MC, Jacobs P, *Hepatic MR imaging with ferumoxides: multicenter study of safety and effectiveness of direct injection protocol.* Radiology, 2003. **228**(2): p. 457-64.

12. Weishaupt D, Willmann JK, Lutz AM, Marincek B, *Resovist for imaging of hepatocellular carcinoma in the cirrhotic liver.* European Radiology, 2004. **14**(Suppl 1): p. C5-6.

13. Bellin MF, Beigelman C, Precetti-Morel S, Precetti-Morel S, *Iron oxide-enhanced MR lymphography: initial experience.* European Journal of Radiology, 2000. **34**(3): p. 257-64.

14. Bellin MF, Roy C, Kinkel K, Thoumas D, Zaim S, Vanel D, Tuchmann C, Richard F, Jacqmin D, Delcourt A, Challier E, Lebret T, Cluzel P, *Lymph node metastases: safety and effectiveness of MR imaging with ultrasmall superparamagnetic iron oxide particles--initial clinical experience.* Radiology, 1998. **207**(3): p. 799-808.

15. Russell M, Anzai Y**,** *Ultrasmall superparamagnetic iron oxide enhanced MR imaging for lymph node metastases.* Radiography, 2007. **13**(Supplement 1): p. e73-e84

16. Corot C, Petry KG, Trivedi R, Saleh A, Jonkmanns C, Le Bas JF, Blezer E, Rausch M, Brochet B, Foster-Gareau P, Balériaux D, Gaillard S, Dousset V., *Macrophage imaging in central nervous system and in carotid atherosclerotic plaque imaging using ultrasmall superparamagnetic iron oxide in magnetic resonance imaging.* Investigative Radiology, 2004. **39** p. (619-25).

17. Herborn CU, Vogt FM, Lauenstein TC, Dirsch O, Corot C, Robert P, Ruehm SG, *Magnetic resonance imaging of experimental atherosclerotic plaque: comparison of two ultrasmall superparamagnetic particles of iron oxide.* Journal of Magnetic Resonance Imaging, 2006. **24**(2): p. 388-93.

18. Kleinschnitz C, Bendszus M, Frank M, Solymosi L, Toyka KV, Stoll G, *In vivo monitoring of macrophage infiltration in experimental ischemic brain lesions by magnetic resonance imaging.* Journal of Cerebral Blood Flow and Metabolism: official journal of the International Society of Cerebral Blood Flow and Metabolism, 2003. **23**(11): p. 1356-61.

19. Benderbous S, Corot C, Jacobs P, Bonnemain B, *Superparamagnetic agents: physicochemical characteristics and preclinical imaging evaluation.* Academic Radiology, 1996. **3**(Suppl 2): p. S292-4.

20. Bernas LM, Foster PJ, and Rutt BK, *Magnetic resonance imaging of in vitro glioma cell invasion.* Journal of Neurosurgery, 2007. **106**(2): p. 306-13.

21. Delo DM, Olson J, Baptista PM, D'Agostino RB Jr, Atala A, Zhu JM, Soker S, *Non-Invasive Longitudinal Tracking of Human Amniotic Fluid Stem Cells in the Mouse Heart.* Stem Cells Development, 2008. **In Press, Corrected Proof.**

22. Raschzok N, Morgul MH, Pinkernelle J, Vondran FW, Billecke N, Kammer NN, Pless G, Adonopoulou MK, Leist C, Stelter L, Teichgraber U, Schwartlander R, Sauer IM, *Imaging of Primary Human Hepatocytes Using Micron-Sized Iron Oxide Particles and Clinical Magnetic Resonance Tomography.* Journal of Cellular and Molecular Medicine, 2008. **In Press, Corrected Proof.**

23. Valable S, Barbier EL, Bernaudin M, Roussel S, Segebarth C, Petit E, Rémy C, *In vivo MRI tracking of exogenous monocytes/macrophages targeting brain tumors in a rat model of glioma.* NeuroImage, 2008. **40**(2): p. 973-83.

24. von zur Muhlen C, von Elverfeldt D, Moeller JA, Choudhury RP, Paul D, Hagemeyer CE, Olschewski M, Becker A, Neudorfer I, Bassler N, Schwarz M, Bode C, Peter K, *Magnetic resonance imaging contrast agent targeted toward activated platelets allows in vivo detection of thrombosis and monitoring of thrombolysis.* Circulation, 2008. **118**(3): p. 258-67.

25. Kiessling F, *Noninvasive cell tracking.* Handbook of Experimental Pharmacology, 2008(185 Pt 2): p. 305-21.

26. Kim J, Kim DI, Lee SK, Kim DJ, Lee JE, Ahn SK, *Imaging of the inflammatory response in reperfusion injury after transient cerebral ischemia in rats: correlation of superparamagnetic iron oxide-enhanced magnetic resonance imaging with histopathology.* Acta Radiologica, 2008. **49**(5): p. 580-8.

27. Stoll G, Bendszus M, *Imaging of inflammation in the peripheral and central nervous system by magnetic resonance imaging.* Neuroscience, 2008. **In Press, Corrected Proof.**

28. Bierry G, Jehl F, Boehm N, Robert P, Prévost G, Dietemann JL, Desal H, Kremer S, *Macrophage activity in infected areas of an experimental vertebral osteomyelitis model: USPIO-enhanced MR imaging--feasibility study.* Radiology, 2008. **248**(1): p. 114-23.

29. Karen CBS, Venkatesh M, Fabien H, Christophe CJ, Zahi AF, *Fractionated Feridex and positive contrast: in vivo MR imaging of atherosclerosis.* Magnetic Resonance Medicine, 2008. **59**(4): p. 721-30.

30. Chang HH, Moura JMF, Wu YL, Ho C, *Automatic detection of regional heart rejection in USPIO-enhanced MRI.* IEEE Transactions on Medical Imaging, 2008. **27**(8): p. 1095-106.

31. Gambarota G, Leenders W, Maass C, Wesseling P, van der Kogel B, van Tellingen O, Heerschap A, *Characterisation of tumour vasculature in mouse brain by USPIO contrast-enhanced MRI.* British Journal of Cancer, 2008. **98**(11): p. 1784-9.

32. Williams JB, Ye Q, Hitchens TK, Kaufman CL, Ho C, *MRI detection of macrophages labeled using micrometer-sized iron oxide particles.* Journal of Magnetic Resonance Imaging, 2007. **25**(6): p. 1120-8.

33. Bourrinet P, Bengele HH, Bonnemain B, Dencausse A, Idee JM, Jacobs PM, Lewis JM, *Preclinical safety and pharmacokinetic profile of ferumoxtran-10, an ultrasmall superparamagnetic iron oxide magnetic resonance contrast agent.* Investigative Radiology, 2006. **41**(3): p. 313-24.

34. Weissleder R, Stark DD, Engelstad BL, Bacon BR, Compton CC, White DL, Jacobs P, Lewis J, *Superparamagnetic iron oxide: pharmacokinetics and toxicity.* AJR American Journal of Roentgenology, 1989. **152**(1): p. 167-73.

35. Bonnemain B, *Superparamagnetic agents in magnetic resonance imaging: physicochemical characteristics and clinical applications. A review.* Journal of Drug Target, 1998. **6**(3): p. 167-74.

36. Wang YX, H SM, Krestin GP, *Superparamagnetic iron oxide contrast agents: physicochemical characteristics and applications in MR imaging.* European Radiology, 2001. **11**(11): p. 2319-31.

37. Rausch M, Hiestand P, Baumann D, Cannet C, Rudin M, *MRI-based monitoring of inflammation and tissue damage in acute and chronic relapsing EAE.* Magnetic Resonance in Medicine, 2003. **50**(2): p. 309-14.

38. Dousset V, Delalande C, Ballarino L, Quesson B, Seilhan D, Coussemacq M, Thiaudiére E, Brochet B, Canioni P, Caillé JM, *In vivo macrophage activity imaging in the central nervous system detected by magnetic resonance.* Magnetic Resonance in Medicine, 1999. **41**(2): p. 329-33.

39. Rausch M, Sauter A, Fröhlich J, Neubacher U, Radü EW, Rudin M, *Dynamic patterns of USPIO enhancement can be observed in macrophages after ischemic brain damage.* Magnetic Resonance in Medicine, 2001. **46**(5): p. 1018-22.

40. Saleh A, Schroeter M, Jonkmanns C, Hartung HP, Mödder U, Jander S, *In vivo MRI of brain inflammation in human ischaemic stroke.* Brain, 2004. **127**(Pt 7): p. 1670-7.

41. Saleh A, Wiedermann D, Schroeter M, Jonkmanns C, Jander S, Hoehn M, *Central nervous system inflammatory response after cerebral infarction as detected by magnetic resonance imaging.* Nuclear Magnetic Resonance in Biomedicine, 2004. **17**(4): p. 163-9.

42. Durand E, Raynaud JS, Bruneval P, Brigger I, Al Haj Zen A, Mandet C, Lancelot E, Lafont A, *Magnetic resonance imaging of ruptured plaques in the rabbit with ultrasmall superparamagnetic particles of iron oxide.* Journal of Vascular Research, 2007. **44**(2): p. 119-28.

43. Kooi ME, Cappendijk VC, Cleutjens KB, Kessels AG, Kitslaar PJ, Borgers M, Frederik PM, Daemen MJ, van Engelshoven JM, *Accumulation of ultrasmall superparamagnetic particles of iron oxide in human atherosclerotic plaques can be detected by in vivo magnetic resonance imaging.* Circulation, 2003. **107**(19): p. 2453-8.

44. Wu YL, Ye Q, Foley LM, Hitchens TK, Sato K, Williams JB, Ho C, *In situ labeling of immune cells with iron oxide particles: an approach to detect organ rejection by cellular MRI.* Proceedings of the National Academy of Sciences of the United States of America, 2006. **103**(6): p. 1852-7.

45. Kanno S, Wu YJ, Lee PC, Dodd SJ, Williams M, Griffith BP, Ho C, *Macrophage accumulation associated with rat cardiac allograft rejection detected by magnetic resonance imaging with ultrasmall superparamagnetic iron oxide particles.* Circulation, 2001. **104**(8): p. 934-8.

46. Shapiro EM, Skrtic S, Sharer K, Hill JM, Dunbar CE, Koretsky AP, *MRI detection of single particles for cellular imaging.* Proceedings of the National Academy of Sciences of the United States of America, 2004. **101**(30): p. 10901-6.

47. Lewin M, Carlesso N, Tung CH, Tang XW, Cory D, Scadden DT, Weissleder R, *Tat peptide-derivatized magnetic nanoparticles allow in vivo tracking and recovery of progenitor cells.* Nature Biotechnology, 2000. **18**(4): p. 410-4.

48. Bulte JW, Douglas T, Witwer B, Zhang SC, Strable E, Lewis BK, Zywicke H, Miller B, van Gelderen P, Moskowitz BM, Duncan ID, Frank JA, *Magnetodendrimers allow endosomal magnetic labeling and in vivo tracking of stem cells.* Nature Biotechnology, 2001. **19**(12): p. 1141-7.

49. Brekke C, Williams SC, Price J, Thorsen F, Modo M, *Cellular multiparametric MRI of neural stem cell therapy in a rat glioma model.* NeuroImage, 2007. **37**(3): p. 769-82.

50. Frangogiannis NG, Smith CW, Entman ML, *The inflammatory response in myocardial infarction.* Cardiovascular Research, 2002. **53**(1): p. 31-47.

51. Ren G, Dewald O, Frangogiannis NG, *Inflammatory mechanisms in myocardial infarction.* Current Drug Targets - Inflammation & Allergy, 2003. **2**(3): p. 242-56.

52. Frangogiannis NG, *The mechanistic basis of infarct healing.* Antioxidants & Redox Signaling, 2006. **8**(11-12): p. 1907-39.

53. Timmers L, Sluijter JP, van Keulen JK, Hoefer IE, Nederhoff MG, Goumans MJ, Doevendans PA, van Echteld CJ, Joles JA, Quax PH, Piek JJ, Pasterkamp G, de Kleijn DP, *Toll-like receptor 4 mediates maladaptive left ventricular remodeling and impairs cardiac function after myocardial infarction.* Circulation Research, 2008. **102**(2): p. 257-64.

54. Leor J, Rozen L, Zuloff-Shani A, Feinberg MS, Amsalem Y, Barbash IM, Kachel E, Holbova R, Mardor Y, Daniels D, Ocherashvilli A, Orenstein A, Danon D, *Ex vivo activated human macrophages improve healing, remodeling, and function of the infarcted heart.* Circulation, 2006. **114**(1 Suppl): p. I94-100.

55. Sosnovik DE, Nahrendorf M, Deliolanis N, Novikov M, Aikawa E, Josephson L, Rosenzweig A, Weissleder R, Ntziachristos V, *Fluorescence tomography and magnetic resonance imaging of myocardial macrophage infiltration in infarcted myocardium in vivo.* Circulation, 2007. **115**(11): p. 1384-91.